Int Nano Lett (2017) 7:187–193
DOI 10.1007/s40089-017-0213-3

ORIGINAL ARTICLE

Synthesis of CeO_2-based core/shell nanoparticles with high oxygen storage capacity

Aytekin Uzunoglu[1,2] · **Dursun Ali Kose**[3] · **Lia A. Stanciu**[1,4]

Received: 7 March 2017 / Accepted: 11 July 2017 / Published online: 17 July 2017

Abstract Ceria plays a key role in various applications including sensing and catalysis owing to its high oxygen storage capacity (OSC). The aim of this work is to prepare novel MO_x/CeO_2 (M: Zr, Ti, Cu) metal oxide systems with core/shell structures using a facile two-step chemical precipitation method. The synthesized nanoparticles were characterized using X-ray diffraction (XRD), transmission electron microscopy (TEM), and N_2 adsorption methods. The OSC property of the samples was evaluated using TGA analysis conducted at 600 °C under reductive (5% H_2/Ar) and oxidative (synthetic air) environments. The OSCs of the samples were found to be 130, 253, and 2098 μmol-O_2/g for ZrO_2/CeO_2, TiO_2/CeO_2, and CuO/CeO_2, respectively. Effects of heat treatment on the physical and redox properties of the samples were also evaluated. In this regard, the samples were exposed to 500 °C for 5 h under ambient environment. It was observed that the heat treatment induced the formation of mixed metal oxide alloys and the BET surface area of the samples diminished significantly. The OSC of the samples, however, did not experience any significant chance, which was attributed to the compensation of the loss in the surface area by the alloy formation after the heat treatment.

✉ Aytekin Uzunoglu
aytekingyte@gmail.com; aytekinuzunoglu@hitit.edu.tr

[1] School of Materials Engineering, Purdue University, West Lafayette, IN 47907, USA

[2] Alaca Avni Celik Vocational School, Hitit University, 19600 Alaca, Corum, Turkey

[3] Department of Chemistry, Faculty of Science and Arts, Hitit University, 19030 Corum, Turkey

[4] Weldon School of Biomedical Engineering, Purdue University, West Lafayette, IN 47907, USA

Keywords CeO_2 · Core/shell · Oxygen storage capacity · Nanoparticles · ZrO_2 · TiO_2 · CuO

Introduction

Ceria (CeO_2) and ceria-based nanomaterials have attracted great deal of interest for many applications ranging from cosmetic and sensing to catalysis due to their high redox properties [1–5]. The high redox property of CeO_2, which is also called as oxygen storage capacity (OSC), originates from the capability of binding O_2 reversibly by shifting from Ce^{3+} to Ce^{4+} states under oxygen-rich and oxygen-lean environments, respectively [3, 6]. Its high OSC property makes CeO_2-based materials one of the key components in three-way catalysts in the automotive industry. It is known that the exhaust gas has fluctuations in O_2 content and the concentration of O_2 in the gas stream goes down and up, resulting from deviations in the stoichiometric air/fuel ratio. To remove the pollutants from the exhaust gas effectively, the stoichiometric ratio must be maintained [7]. The use of CeO_2-based materials in three-way catalyst systems as a promoter ensures the maintenance of the air/fuel stoichiometry by acting as oxygen buffer under the mentioned conditions. The reversible oxygen release and uptake property of CeO_2 is shown in Eq. 1 [8].

$$2CeO_2 \leftrightarrow Ce_2O_3 + 1/2\ O_2. \quad (1)$$

It was reported that the OSC property is highly depended upon the morphology, composition, and the physical surface area of CeO_2 [9, 10]. The modification of CeO_2 lattice with dissimilar ions yields enhanced OSC by creating additional O_2 defects in the structure, which results in higher O_2 mobility. The introduction of Zr^{4+} ions into the

CeO_2 lattice, for example, produces higher oxygen defects in the structure in quantity due to the formation of distortions in the fluorite-type structure of CeO_2. These distortions are associated with the difference in the ionic radius of Ce^{4+} and Zr^{+4} [11, 12]. The modification of the lattice with secondary ions such as Cu^{2+} with different oxidation states than Ce^{4+} leads to the formation of additional structural defects associated with the neutralization of the total charge in the mixed metal oxide system [7]. In our previous work, we showed that the formation of the additional structural defects is beneficial for enhanced lattice oxygen transport which in turn results in higher OSC [7]. It was also reported that the enlarged physical surface area renders higher OSC [13, 14]. That is reason of having higher redox property with CeO_2 and CeO_2-based nanoparticles compared to those obtained from their bulk counterparts.

Despite its high OSC property, pristine CeO_2 is not favorable to be used in high-temperature applications, especially in three-way catalysis, owing to its low thermal stability. At high temperatures, the OSC of CeO_2 and CeO_2-based materials was reported to be deactivated due to the sintering effect and phase separation [15–17]. The modification of CeO_2 lattice with secondary metal oxide systems, especially ZrO_2, was found to be an effective way to enhance the thermal stability of these materials [8]. Although a great deal of attention has been paid to develop novel CeO_2-based materials with higher thermal stability and sintering resistance, the decrease in the physical surface area of these catalytic materials is still a major challenge for high-temperature applications.

In this work, we aimed to prepare novel MO_x/CeO_2 (M: Zr, Ti, Cu) metal oxide systems with core/shell structure using a facile two-step chemical precipitation method. To the best of our knowledge, the synthesis and characterization of these MO_x/CeO_2 core/shell structures with high oxygen storage capacity have not been reported yet. For this purpose, first, MO_x nanoparticles were synthesized and used as seeds for the formation of CeO_2 shells. The prepared core/shell nanoparticles were then physically characterized to using X-ray diffraction (XRD), transmission electron microscopy (TEM), and N_2 adsorption (BET) methods. Moreover, the OSC of the fresh and calcined samples was measured to determine the effect of the composition on the OSC and the thermal stability of the nanoparticles.

Materials and methods

Materials

$TiCl_4$ (99.0%) was purchased from Fluka. Reducing agent, NH_4OH (28–30%), was bought from Science Lab. Ce $(NO_3)_3{\cdot}xH_2O$ (99.999%), $N_2O_7Zr{\cdot}xH_2O$ (99.0%), $CuN_2O_6{\cdot}xH_2O$ (99.999%), NaOH were obtained from Aldrich. The chemicals were used as received.

Preparation of core/shell nanoparticles

MO_x nanoparticles used as core in the core–shell structure was prepared via a chemical precipitation method conducted at room temperature. Briefly, required amounts of MO_x (M: Zr, Ti, Cu) precursor were dissolved in distilled water to prepare 0.1 M stock solution. While 100 mL of metal oxide solution was stirring vigorously using a magnetic stirrer, excessive NH_4OH solution (4 M, 0.25 mL) was added to the solution dropwise. The resulting solution was stirred for 1 more hour and left for aging overnight. MO_x nanoparticles were collected by centrifuging after washing the nanoparticles five times with deionized water. Then, the nanoparticles were dried at 100 °C overnight and calcined for 5 h at 500 °C.

The synthesis of the core/shell nanoparticles was reported by Kanmani and Ramachandran [18]. Briefly, the prepared MO_x nanoparticles were dispersed in an aqueous $Ce(NO_3)_3{\cdot}xH_2O$ solution. The molar ratio of Ce^{4+} to M^{n+} was set to 1/1. After homogenization of the solution, 0.1 M NaOH solution (250 ml) was added to the precursor-containing beaker dropwise. The resultant mixture was left stirring for 5 h at room temperature to obtain a good dispersion. After that, the solution was stirred three more hours at 97 °C to form the core/shell structure.

Characterization of core/shell nanoparticles

X-ray diffraction (XRD) data of the samples were recorded using a Bruker D8 Focus X-ray Diffractometer equipped with Cu Kα ($\lambda = 0.15406$ nm) radiation. The XRD scans were conducted at the scan rate of 4° min^{-1} over 2θ values between 20° and 70°. Debye–Scherrer equation was implemented to calculate the average crystalline size of the core/shell nanoparticles. An FEI Tecnai TEM operating at 200 kV was used to take the TEM images. The physical surface area of the samples was measured using N_2 adsorption–desorption analysis performed at −196 °C (a TriStar 300). Prior to the physisorption, the nanoparticles were degassed at 300 °C for 3 h.

The oxygen storage capacity of the core/shell nanoparticles was measured using an SDT 2960 DTA–TGA from TA Instruments. The samples were heated to 600 °C under reductive environment (5% H_2/Ar, 100 mL/min) and waited until the mass of the sample stabilized. Then, oxidative (synthetic air) and reductive gases were fed to the sample alternatively and the mass change was used to calculate the average OSC in μmol-O_2/g powder.

Results and discussions

Figure 1 shows the XRD results of the as-prepared core/shell ZrO_2/CeO_2, TiO_2/CeO_2, and CuO/CeO_2 nanoparticles. The peaks located at ca. 28.6°, 33.4°, 47.6°, and 56.6° correspond to the fluorite-type structure of CeO_2 (JCPDS 34-0394). For all core/shell compositions, secondary fluorite-type CeO_2 was observed showing the successful coating of MO_x nanoseeds with CeO_2 by a simple two-step precipitation method without the use of any surfactant. MgO peaks indicated with asterisks in the XRD patters were used to have a standard to adjust the peak locations precisely to avoid any possible calculation errors in lattice parameters and average crystalline sizes. The XRD signals located at around 31.5° and 50.3° ascribed to tetragonal ZrO_2 phase. In addition, the XRD patterns of TiO_2/CeO_2 and CuO/CeO_2 core/shell metal oxide systems revealed the presence of rutile TiO_2 and monoclinic CuO phases, respectively. The corresponding XRD signals are shown in Fig. 1. The lattice parameter of CeO_2 coating was calculated using the XRD signal obtained from (220) peak because the first two CeO_2 peaks were interfered by the XRD signals of core phases. The lattice parameter values calculated using the Scherer's equation were close to each other with a slight deviation for TiO_2/CeO_2 core–shell (Table 1). It is due to the fact that fresh samples were not exposed to any heat treatment which may result in the formation of mixed metal oxides. The physical surface area values of the core–shell nanoparticles were found to be 103.8, 100.6, and 131.9 $m^2\ g^{-1}$ for ZrO_2/CeO_2, TiO_2/CeO_2, and CuO/CeO_2 nanoparticles, respectively. The results indicated that the modification of CuO surface with CeO_2 yielded the largest surface area among all samples, which is crucial for the enhanced OSC property.

The morphology of the samples was studied using transmission electron microscopy (TEM). The TEM images taken at high magnifications are shown in Fig. 2. It was

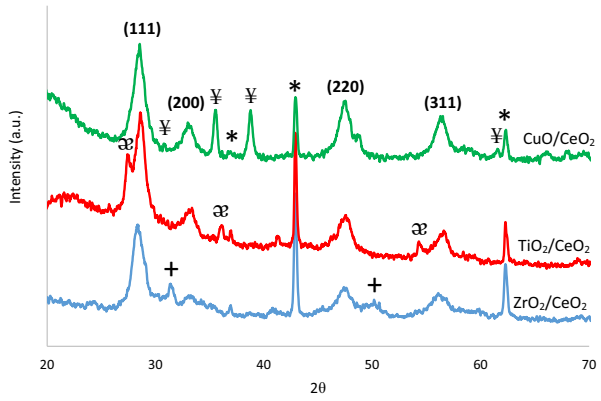

Fig. 1 XRD patterns of as-prepared core/shell nanoparticles (*: MgO, +: tetragonal ZrO_2, æ: rutile TiO_2, and ¥: monoclinic CuO)

Table 1 Physical surface area, average crystalline size, and the lattice parameter values of the as-prepared core/shell nanoparticles

Sample	BET surface area ($m^2\ g^{-1}$)	CeO_2 lattice parameter, a (Å)	Average crystalline size of CeO_2 (nm)
ZrO_2/CeO_2	103.8	5.43	17.3
TiO_2/CeO_2	100.6	5.38	12.8
CuO/CeO_2	131.9	5.41	8.1

observed that the shape of the nanoparticles was irregular and deviated from spherical shape. As seen from the figure, the CuO/CeO_2 composition had the smallest average particle size. Due to the similar contrasts of different metal oxide phases under the electron beam, it was not possible to see the core/shell structure clearly. To shed light on the core/shell structure, the inter-planar distance values shown in Fig. 2b, d, f were used. The inter-planar distance of 0.31 nm corresponds to (111) plane of the fluorite-type CeO_2 structure [19]. The inter-planar distance values of 0.29, 0.35, and 0.25 nm are associated with ZrO_2 (111) [20], TiO_2 (101) [21], and CuO (002) [22] planes, respectively. This result indicated that the CeO_2 layer covered the surface of the MO_x agglomerates. While the inner region of the agglomerates was rich in MO_x, the outer layer was dominated by the CeO_2 shell, showing the formation of core/shell structure.

The OSC of the core/shell nanoparticles was calculated using the change in the mass resulted from the release and uptake of oxygen atoms from the structure (Fig. 3) [2, 23, 24]. The TGA curves are shown in Fig. 3. It was observed that compared to our previous report [7], the core–shell design of ZrO_2/CeO_2 metal oxide nanoparticles resulted in a significant increase in the OSC of CeO_2. The lowest oxygen storage capacity, however, was obtained from this composition among all synthesized samples. The OSC of the samples followed the order of ZrO_2/CeO_2 $< TiO_2/CeO_2 < CuO/CeO_2$ with the calculated values of 130, 253, and 2098 μmol-O_2/g, respectively. Since the samples were not exposed to any heat treatment which may result in the formation of mixed metal oxide alloys, the enhanced OSC may be attributed to the larger physical surface area of the samples. While pristine CeO_2 had the BET surface area of 55.7 $m^2\ g^{-1}$ (reported in our previous study), the core/shell design yielded much larger surface area exposing higher number of CeO_2 lattice on the surface. Since CeO_2 surface play a key role in the oxygen release and uptake property, higher number of exposed CeO_2 structures is accounted for the increased OSC. It is also noteworthy that when the XRD signals of pristine CeO_2 and core–shell nanoparticles were compared (not shown here), there were no significant shifts in the (111) peak locations of CeO_2 showing no alloying effect of MO_x in the CeO_2 lattice. This result confirmed that the enhanced

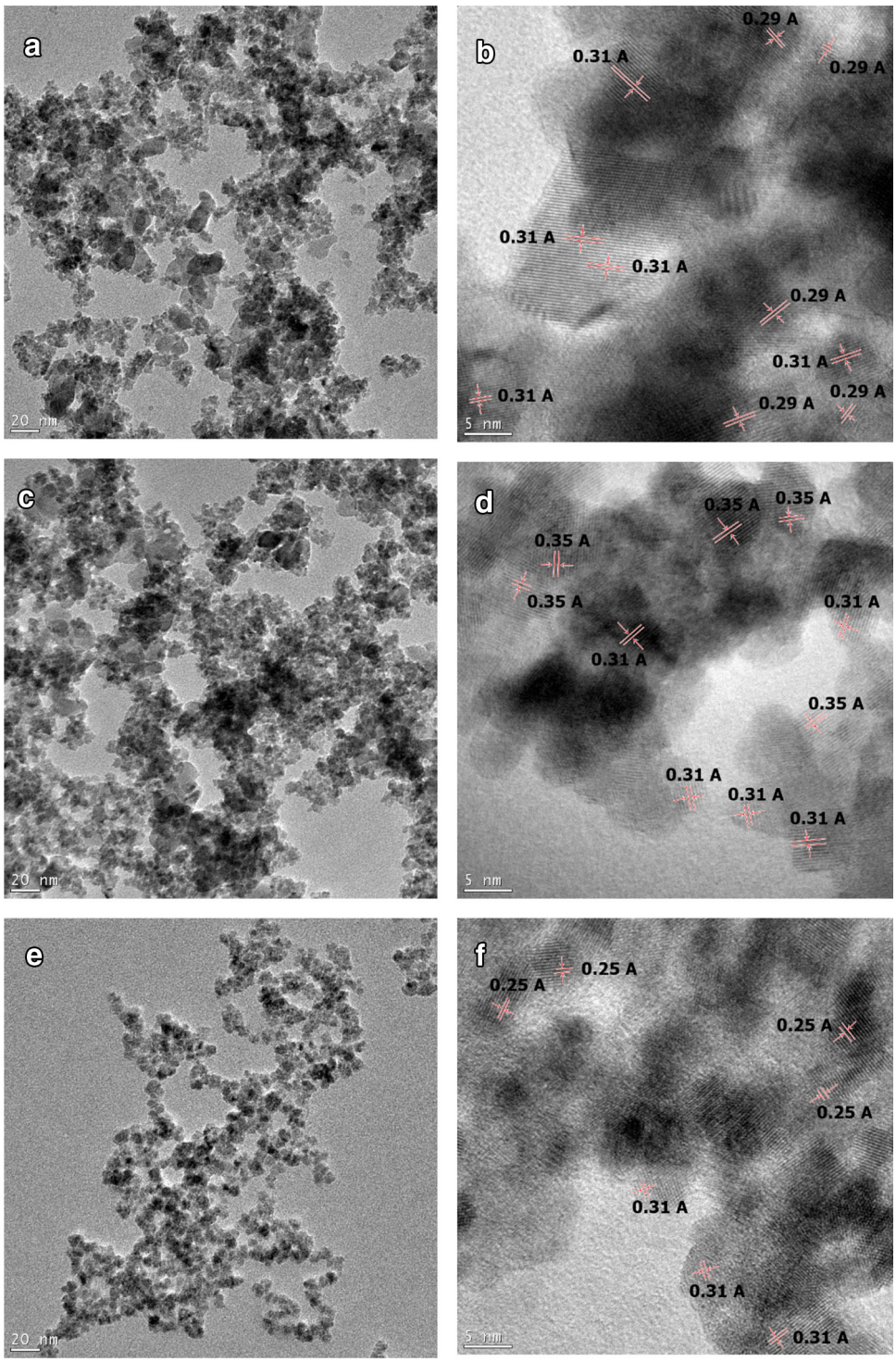

Fig. 2 TEM images of the samples **a**, **b** ZrO_2/CeO_2, **c**, **d** TiO_2/CeO_2, and **e**, **f** CuO/CeO_2

OSC values were mainly due to the enlarged surface area. When the calculated OSC values of the core/shell nanoparticles were compared with those obtained from theoretical calculation (listed in Table 2), it is essential to note that the OSC of CuO/CeO_2 system was even higher than the theoretical value. This can be explained by the presence of distinctive monoclinic CuO phase which has a very high redox property. Besides the CeO_2 phase, the monoclinic CuO phase contributed to the OSC.

The prepared core/shell nanoparticles were calcined at 500 °C for 5 h under ambient atmosphere to evaluate the effects of heat treatment on the structure and OSC property

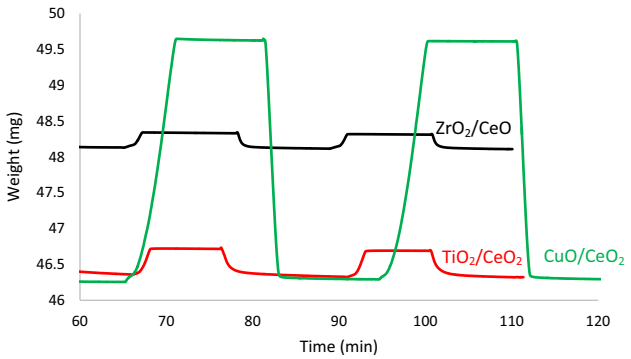

Fig. 3 TGA results of the fresh samples under oxidative and reductive environments at the temperature of 600 °C

Table 2 OSC values of the fresh samples calculated from the TGA data

Sample	BET surface area (m^2 g^{-1})	OSC (μmol-O_2/g)	Theoretical OSC (μmol-O_2/g)[a]
ZrO_2/CeO_2	103.8	130	846
TiO_2/CeO_2	100.6	253	992
CuO/CeO_2	131.9	2098	992

[a] Theoretical contribution of CeO_2 calculated based on Eq. 1

of the samples. After the calcination process, the samples were characterized using XRD, N_2 adsorption, and TGA experiments.

The lattice parameter values and the average crystalline sizes of the fresh and aged samples are listed in Table 3. It was observed that after the heat treatment, although it is expected to have higher crystalline size values due to the sintering effect, the average crystalline size of the CeO_2 decreased for all compositions but CuO/CeO_2. This is due to the fact that the XRD peaks of MO_x (Cu, Zr, Ti) are located at the close proximity to the characteristic CeO_2 peaks, resulting in the formation of shoulders in the CeO_2 signal. Due to this broadening effect, the FWHF values used to calculate the average crystalline size could not be determined precisely, which is responsible for the discrepancy in the calculated lattice parameter and average crystalline size values. Therefore, it will be wise to use the physical surface area values and location of the XRD peaks to evaluate the heat treatment effect on the physical properties of the core–shell nanoparticles. The XRD results of the calcined samples are shown in Fig. 4a–c. It was observed that after the heat treatment, the characteristic peaks of the fluorite-type CeO_2 structure shifted to higher 2θ values, confirming the formation of CeO_2–MO_x solid solution. In addition to these shifts induced by the heat treatment, the peaks became narrower and sharper, which indicated larger average crystalline size. The BET surface area of the calcined samples is listed in Table 4. Calcination of the core–shell nanoparticles induced a high degree of drop in the physical surface area. As expected, the CuO-containing composition experienced the highest drop in the surface area which was due to the low sintering resistance of CuO and CeO_2 phases. The higher thermal stability of ZrO_2- and TiO_2-containing samples is attributed to the interaction of Zr^{4+} and Ti^{4+} ions with Ce^{4+} in the lattice [7].

The OSC performance of the calcined samples is listed in Table 4. It must be mentioned that although the physical surface area of the samples showed a significant drop with the calcination process, the same effect was not observed for the OSC properties of the core/shell nanoparticles. All the core/shell compositions showed similar OSC properties with their fresh counterparts after the calcination process. The TGA results of the calcined samples are shown in Fig. 5. The results demonstrated that as mentioned earlier, the OSC of CeO_2 nanoparticles is governed not only by the physical surface area but also by the structural properties. The XRD patterns indicated the formation of metal oxide alloys by the shift in the characteristic peak locations. The formation of CeO_2–MO_x mixed metal oxide alloys induces the formation of additional structural defects including oxygen defects and distortions in the CeO_2 lattice. These additional defects are responsible for the maintenance of the high OSC properties of the calcined samples. In other words, the detrimental effect of the surface area drop by calcination was compensated by the increased number of structural defects, resulting in the maintenance of the OSC values.

Conclusions

In this work, ZrO_2/CeO_2, TiO_2/CeO_2, and CuO/CeO_2 core/shell nanoparticles were successfully synthesized via a two-step chemical precipitation process without the use of

Table 3 Physical surface area, average crystalline size, and the lattice parameter values of the as-prepared and calcined core/shell nanoparticles

Sample	CeO_2 lattice parameter, a (Å)	CeO_2 lattice parameter after calcination, a (Å)	Average crystalline size of CeO_2 (nm)	Average crystalline size of CeO_2 after calcination (nm)
ZrO_2/CeO_2	5.43	5.42	17.3	12.7
TiO_2/CeO_2	5.38	5.42	12.8	11.5
CuO/CeO_2	5.41	5.41	8.1	10.6

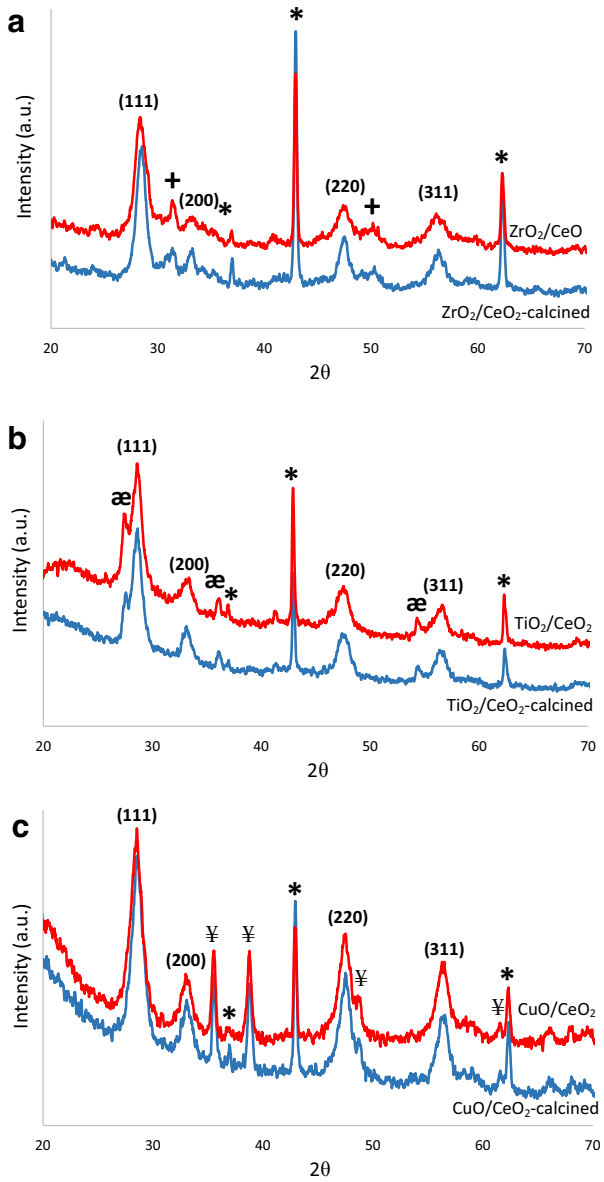

Fig. 4 XRD patterns of fresh and calcined **a** ZrO_2/CeO_2, **b** TiO_2/CeO_2, and **c** CuO/CeO_2 nanoparticles (*: MgO, +: tetragonal ZrO_2, æ: rutile TiO_2, and ¥: monoclinic CuO)

any surfactant. The XRD results indicated the presence of CeO_2 and MO_x (M: Zr, Ti, Cu) phases. The physical surface area of the samples was determined to be 103.8, 100.6, and 131.9 $m^2\ g^{-1}$ for ZrO_2/CeO_2, TiO_2/CeO_2, and CuO/CeO_2 nanoparticles, respectively, which were larger than that of pristine CeO_2. The core/shell structure of the samples was analyzed using TEM, and the images confirmed the formation of core–shell structures. The OSC of the samples followed the order of $ZrO_2/CeO_2 < TiO_2/CeO_2 < CuO/CeO_2$ with the calculated values of 130, 253, and 2098 μmol-O_2/g, respectively. The enhanced OSC of the core/shell nanoparticles was mainly attributed to the larger surface. The effect of heat treatment on the properties of the samples was evaluated by calcining the samples at 500 °C for 5 h under ambient atmosphere. The XRD peaks of the samples shifted to higher 2θ values showing the formation of CeO_2–MO_x mixed metal oxide alloys. The physical surface area of the samples, however, diminished after the calcination process. While the benefit of having large surface area for the enhanced OSC was lost after the heat treatment, the formation of metal oxide alloys yielded additional structural defects, resulting in the maintenance of the enhanced OSC.

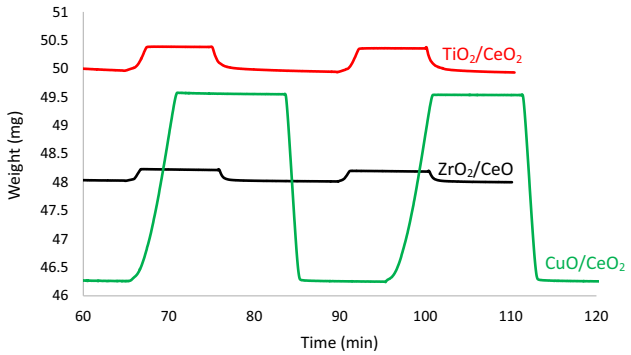

Fig. 5 TGA results of the heat-treated samples under oxidative and reductive environments at 600 °C

Table 4 OSC and BET surface area values of the fresh and calcined samples

Sample	BET surface area of fresh sample ($m^2\ g^{-1}$)	BET surface area of calcined sample ($m^2\ g^{-1}$)	OSC of fresh sample (μmol-O_2/g)	OSC of calcined sample (μmol-O_2/g)	Theoretical OSC (μmol-O_2/g)[a]
ZrO_2/CeO_2	103.8	70.6	130	120	846
TiO_2/CeO_2	100.6	62.7	253	255	992
CuO/CeO_2	131.9	74.99	2098	2076	992

[a] Theoretical contribution of CeO_2 calculated based on Eq. 1

Compliance with ethical standards

Conflict of interest The authors declare no conflict of interest.

References

1. Uzunoglu, A., Stanciu, L.: Novel CeO_2–CuO-decorated enzymatic lactate biosensors operating in low oxygen environments. Anal. Chim. Acta **909**, 121–128 (2016)
2. Dong, Q., Yin, S., Guo, C.S., Sato, T.: $Ce0.5Zr0.4Sn0.1O_2/Al_2O_3$ catalysts with enhanced oxygen storage capacity and high CO oxidation activity. Catal. Sci. Technol. **2**, 2521–2524 (2012)
3. Benjaram, M.R., Gode, T., Katta, L.: Nanosized unsupported and alumina-supported ceria–zirconia and ceria–terbia solid solutions for CO oxidation. Chin. J. Catal. **32**, 800–806 (2011)
4. Fu, Q., Weber, A., Flytzani-Stephanopoulos, M.: Nanostructured Au–CeO_2 catalysts for low-temperature water-gas shift. Catal. Lett. **77**, 87–95 (2001)
5. Uzunoglu, A., Ramirez, I., Andreasen, E., Stanciu, L.A.: Layer by layer construction of ascorbate interference-free amperometric lactate biosensors with lactate oxidase, ascorbate oxidase, and ceria nanoparticles. Microchim. Acta **183**, 1667–1675 (2016)
6. Trovarelli, A., Boaro, M., Rocchini, E., de Leitenburg, C., Dolcetti, G.: Some recent developments in the characterization of ceria-based catalysts. J. Alloy. Compd. **323**, 584–591 (2001)
7. Uzunoglu, A., Zhang, H., Andreescu, S., Stanciu, S.: CeO_2–MO_x (M: Zr, Ti, Cu) mixed metal oxides with enhanced oxygen storage capacity. Springer J. Mater. Sci. **50**, 3750–3762 (2015)
8. Sugiura, M.: Oxygen storage materials for automotive catalysts: ceria–zirconia solid solutions. Catal. Surv. Asia **7**, 77–87 (2003)
9. Tschope, A., Ying, J.Y.: Nanocrystalline cerium oxide catalytic materials. Nanophase Mater.: Synth. Prop. Appl. **260**, 781–784 (1994)
10. Wu, X.D., Qing, L., Duan, W.: Role of surface adsorption in fast oxygen storage/release of CeO_2–ZrO_2 mixed oxides. J. Rare Earths **25**, 416–421 (2007)
11. Kim, J.R., Myeong, W.J., Ihm, S.K.: Characteristics in oxygen storage capacity of ceria-zirconia mixed oxides prepared by continuous hydrothermal synthesis in supercritical water. Appl. Catal. B-Environ. **71**, 57–63 (2007)
12. Ran, R., Fan, J., Weng, D.: Microstructure and oxygen storage capacity of Sr-modified Pt/CeO_2–ZrO_2 catalysts. Prog. Nat. Sci.-Mater. Int. **22**, 7–14 (2012)
13. Zhou, G.L., Lan, H., Yang, X.Q., Du, Q.X., Xie, H.M., Fu, M.: Effects of the structure of Ce–Cu catalysts on the catalytic combustion of toluene in air. Ceram. Int. **39**, 3677–3683 (2013)
14. Zhou, G., Shah, P.R., Montini, T., Fornasiero, P., Gorte, R.J.: Oxidation enthalpies for reduction of ceria surfaces. Surf. Sci. **601**, 2512–2519 (2007)
15. Abdollahzadeh-Ghom, S., Zamani, C., Andreu, T., Epifani, M., Morante, J.R.: Improvement of oxygen storage capacity using mesoporous ceria–zirconia solid solutions. Appl. Catal. B-Environ. **108**, 32–38 (2011)
16. Schmieg, S.J., Belton, D.N.: Effect of hydrothermal aging on oxygen storage release and activity in a commercial automotive catalyst. Appl. Catal. B-Environ. **6**, 127–144 (1995)
17. Epifani, M., Andreu, T., Abdollahzadeh-Ghom, S., Arbiol, J., Morante, J.R.: Synthesis of ceria–zirconia nanocrystals with improved microstructural homogeneity and oxygen storage capacity by hydrolytic sol–gel process in coordinating environment. Adv. Funct. Mater. **22**, 2867–2875 (2012)
18. Kanmani, S.S., Ramachandran, K.: Synthesis and characterization of TiO_2/ZnO core/shell nanomaterials for solar cell applications. Renew Energy **43**, 149–156 (2012)
19. Yang, Y.S., Mao, Z., Huang, W.J., Liu, L.H., Li, J.L., Wu, Q.Z.: Redox enzyme-mimicking activities of CeO_2 nanostructures: Intrinsic influence of exposed facets. Sci. Rep. **6**, 35344 (2016)
20. Basahel, S.N., Ali, T.T., Mokhtar, M., Narasimharao, K.: Influence of crystal structure of nanosized ZrO_2 on photocatalytic degradation of methyl orange. Nanoscale Res. Lett. **10**, 73 (2015)
21. Chu, L., Li, L.Y., Su, J., Tu, F.F., Liu, N.S., Gao, Y.H.: A general method for preparing anatase TiO_2 treelike-nanoarrays on various metal wires for fiber dye-sensitized solar cells. Sci. Rep. **4** (2014)
22. Cheng, S.L., Chen, M.F.: Fabrication, characterization, and kinetic study of vertical single-crystalline CuO nanowires on Si substrates. Nanoscale Res. Lett. **7**, 119 (2012)
23. Ouyang, J., Yang, H.M.: Investigation of the oxygen exchange property and oxygen storage capacity of $Ce_xZr_{1-x}O_2$ nanocrystals. J. Phys. Chem. C **113**, 6921–6928 (2009)
24. Chuang, C.C., Hsiang, H.I., Hwang, J.S., Wang, T.S.: Synthesis and characterization of Al_2O_3-$Ce0.5Zr0.5O_2$ powders prepared by chemical coprecipitation method. J. Alloy. Compd. **470**, 387–392 (2009)